Processing, microstructure, and elevated temperature mechanical properties of $MoSi_2$ containing $Er_2Mo_3Si_4$ and Er_2O_3 particles

D. K. Patrick
Department of Materials Science and Engineering, The University of Michigan, Ann Arbor, MI 48109–2136 (USA)
D. C. Van Aken
Department of Metallurgical Engineering, The University of Missouri–Rolla, Rolla, MO 65401–0249 (USA)

(Received December 28, 1993; in revised form March 21, 1994)

Abstract

Powders of $MoSi_2$ containing $Er_2Mo_3Si_4$ and Er_2O_3 particles were produced by ball milling arc-melted buttons of $MoSi_2$ containing 20 vol.% $Er_2Mo_3Si_4$. Two composites with grain diameters of 9 and 16 μm were produced by hot pressing the powders to 98% of theoretical density at 1565 °C and 1650 °C respectively. Some evidence of mechanical alloying was observed, but the majority of the $Er_2Mo_3Si_4$ and Er_2O_3 particles were situated on grain boundaries. Compressive decremental step–strain rate tests were performed in the homologous temperature range of 0.54 T_m to 0.7 T_m (1100–1400 °C) for strain rates ranging from 5×10^{-4} s^{-1} to 1×10^{-6} s^{-1}. Nominal values for the stress exponent, n, and the activation energy for creep, Q, were determined using a constitutive equation for power-law creep. Below 1200 °C, creep was controlled by dislocation climb and glide mechanisms with $n \approx 4.5$ and $Q = 425 \pm 15$ kJ mol^{-1}. At 1300 °C and above, the creep resistance was shown to be grain size dependent with creep resistance increasing with larger grain size.

1. Introduction

One of the major concerns in the development of intermetallics for high temperature structural applications is the cleanliness of the final product and the processing techniques used to produce these materials. It is well known, for example, that standard techniques associated with powder processing of molybdenum disilicide ($MoSi_2$) can lead to substantial amounts of SiO_2 being formed within the consolidated material [1–3]. Although the excellent oxidation resistance of $MoSi_2$ is attributed to the formation of a protective layer of SiO_2 on the surface [4–6], it is believed the presence of a viscous silica phase at grain boundaries at temperatures above 1200 °C is detrimental to high temperature mechanical properties [7–9]. Preparing $MoSi_2$ alloys using pure elemental starting materials or processing in completely inert atmospheres can significantly reduce the SiO_2 content in $MoSi_2$ [3, 10, 11]. Elemental additions of strong oxide or carbide formers have also been successful in reducing the SiO_2 content in commercially available $MoSi_2$ powders [7, 8]. Maloy *et al.* [8] have reported lower SiO_2 contents, higher hot hardness, and improved fracture toughness with the addition of carbon, while Mason *et al.* [12, 13] have reported that minor erbium additions made to $MoSi_2$–Mo_5Si_3 eutectics deoxidized the melt and resulted in the formation of an erbium-rich oxide and a complex silicide ($Er_2Mo_3Si_4$).

The addition of crystalline oxides to $MoSi_2$ has also been shown to improve mechanical properties not only at low temperatures where ductility and fracture toughness are primary concerns, but also at temperatures above 0.5 T_m where creep resistance dominates design considerations [7, 14, 15]. Dispersions of unstabilized and partially-stabilized zirconia (PSZ) particulates have been reported to improve the room temperature fracture toughness through transformation toughening and microcracking mechanisms [14]. Kim *et al.* [15] have also shown that dispersions of Al_2O_3 in $MoSi_2$ can significantly increase the compressive yield strength over that of monolithic $MoSi_2$ at about 1300 °C. However, the effect of these crystalline oxides (ZrO_2 and Al_2O_3) on the creep strength of $MoSi_2$ has not as yet been reported. Gibala *et al.* [7] have investigated $MoSi_2$ reinforced with 20 vol.% CaO particulate and they report slight improvements of creep resistance at about 0.6 T_m.

In a previous investigation by the present authors [16] the compressive creep strength of a $MoSi_2$/$Er_2Mo_3Si_4$/20p (20 vol.% $Er_2Mo_3Si_4$ particulate) composite was reported to be similar to that of a $MoSi_2$/SiC/20w (whisker reinforced) composite above 1200 °C [17, 18]. In that study processing of pure

0921-5093/94/$7.00
SSDI 0921-5093(94)09583-1

elemental molybdenum, silicon, and erbium resulted in a $MoSi_2/(Er_2Mo_3Si_4/Er_2O_3)/20p$ composite with a reduced SiO_2 content. However, the individual contribution of each dispersed phase to the creep strength was not reported. In this paper we further examine the high temperature deformation (creep) behavior of $MoSi_2$ reinforced with $Er_2Mo_3Si_4$ and Er_2O_3 particles. Although the Er-rich oxide phase in previous studies was believed to be Er_2O_3 [12, 16], the crystallographic symmetry and space group of this phase was not determined. Therefore, results of an analytical electron microscopy study are also presented in this paper which confirms that this Er-rich oxide phase is indeed Er_2O_3.

2. Experimental details

Materials for this investigation were prepared by arc-melting pure elemental Mo bar stock (supplied by Mi-Tech Metals, Indianapolis, IN), and Si single crystal stock and Er chips (supplied by Alfa Products/Johnson Matthey Inc, Ward Hill, MA) into 15 gram buttons of $MoSi_2$ and $Er_2Mo_3Si_4$. Arc-melting was carried out on a water-cooled copper hearth in a flowing argon atmosphere. The buttons were broken up, mixed in the correct proportions, and remelted into 15 g buttons of $MoSi_2$ + 20vol.% $Er_2Mo_3Si_4$. These buttons were then ball-milled using 5 mm tungsten carbide balls in freon for 48 h to produce a fine powder (less than 100 μm in diameter). The ball-to-material weight ratio was approximately 5:1. Two powder compacts were then hot-pressed at 1565 °C/30MPa/4h and 1650 °C/30MPa/4h using grafoil-lined graphite dies in a flowing argon atmosphere. The temperature during hot-pressing was monitored continuously throughout the run using an optical pyrometer.

Standard metallographic techniques were used to prepare samples for quantitative analysis. Optical micrographs were obtained under standard lighting, cross-polarized, and Nomarski interference-contrast imaging conditions. Nominal linear sizes ($\bar{L}$) and volume fractions (V_f) of the individual constituent phases were determined by lineal analysis and point counting methods. A 95% confidence level was established using the relationships reported by Hilliard and Cahn [19].

Electron microscopy was carried out at the University of Michigan Electron Microbeam Analysis Laboratory. A Hitachi Model S-520 scanning electron microscope equipped with a Kevex microanalyzer was used for backscattered electron (BSE) imaging and for standardless X-ray energy dispersive spectroscopy (XEDS). Thin foils for transmission electron microscopy were prepared by electropolishing and ion-milling techniques. Electropolishing was accomplished using a Fischione twin-jet electropolisher in a methanol-10 vol.% sulfuric acid solution at −40 °C and 30 V. Foils prepared by ion-milling were first dimpled using a SiC/glycerol slurry and polished with 6 μm diamond paste. Analytical electron microscopy (AEM) was performed using a JEOL 2000FX scanning-transmission electron microscope equipped with a Tracor-Northern TN-5502 analysis system. A horizontally mounted thin window detector was used for standardless XEDS. Convergent beam electron diffraction (CBED) was carried out at 150 keV using a Gatan liquid nitrogen cold-stage.

Hot hardness tests were carried out on arc-melted $Er_2Mo_3Si_4$ and the particulate composite hot pressed at 1565 °C using a Nikon QM-2 hot hardness test machine at temperatures between 23 °C and 1300 °C. All tests were conducted in vacuum. Five indentations were made at each temperature and the average was reported.

Samples for mechanical testing were prepared by initially surface grinding the ends of hot-pressed pellets to insure that the ends of the samples would be parallel. Samples measuring 3.5 mm × 3.5 mm × 7 mm were then sectioned from the compacts using a low-speed diamond saw. All sides were ground with 600 grit SiC paper. Compressive decremental step-strain rate tests were performed on a twin-screw driven Instron Model 4507 test machine equipped with a Centorr furnace. Samples were compressed between SiC platens in a flowing argon atmosphere. Boron nitride was used as a lubricant between the ends of the samples and the platens. Tests were conducted at temperatures of 1100 °C, 1200 °C, 1300 °C, and 1400 °C in order to determine nominal values for the stress exponent, n, and the activation energy for creep, Q, according to the constitutive equation

$$\dot{\varepsilon} = A\sigma^n \exp\left(\frac{-Q}{RT}\right) \tag{1}$$

where A is a material constant, R is the universal gas constant (8.314 J K^{-1} mol^{-1}) and T is the absolute test temperature.

3. Results and discussion

The microstructures of the arc-melted materials are shown in Fig. 1. At 10 vol.% (Fig. 1(a)) a cellular solidification structure was observed with the $Er_2Mo_3Si_4$ forming as a continuous layer between the $MoSi_2$ cells. At 20 vol.% the $Er_2Mo_3Si_4$ grain boundary film was replaced by a eutectic structure (Fig. 1(b)) with small Mo_5Si_3 particles dispersed within the eutectic. Volume

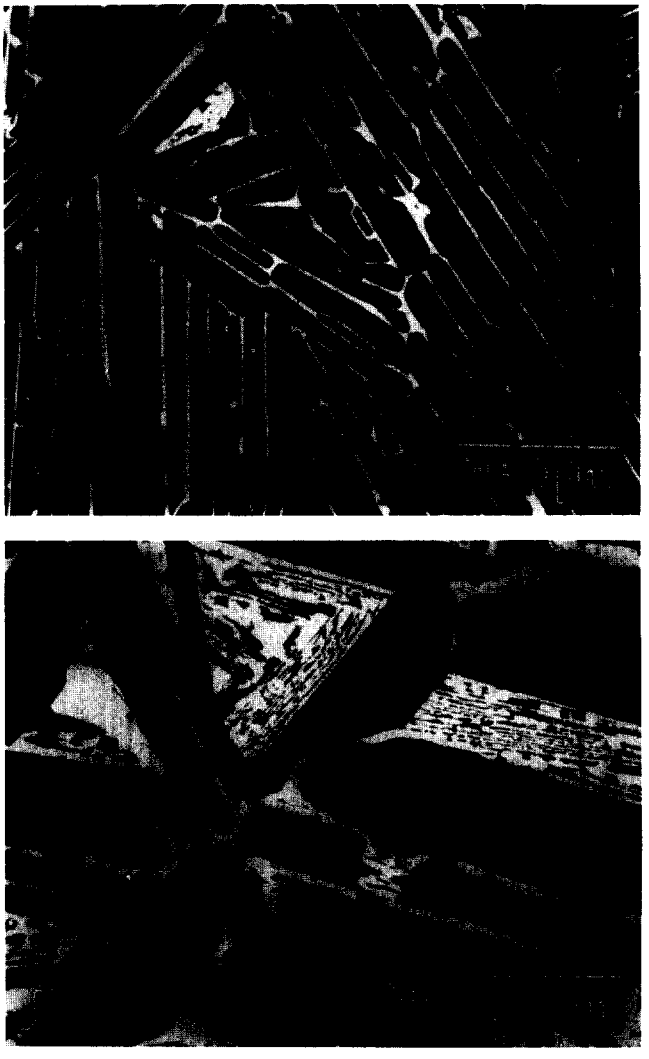

Fig. 1. Backscattered electron micrographs of (a) arc-melted $MoSi_2$ + 10 vol.% $Er_2Mo_3Si_4$, and (b) arc-melted $MoSi_2$ + 20 vol.% $Er_2Mo_3Si_4$. In the 10 vol.% material the $Er_2Mo_3Si_4$ forms as a continuous, thin grain boundary layer, while in the 20 vol. % material a eutectic structure has formed on the boundary containing $MoSi_2$, $Er_2Mo_3Si_4$, and small particles of Mo_5Si_3. Phases are identified as: A, $MoSi_2$, B, $Er_2Mo_3Si_4$, and C, Mo_5Si_3.

Fig. 2. Backscattered electron images of (a) an Er_2O_3 particle seen after breaking up an $Er_2Mo_3Si_4$ button prior to mixing and re-melting with $MoSi_2$. The light phase is $Er_2Mo_3Si_4$. (b) After ball-milling for 48 h the remelted $MoSi_2$ + 20 vol.% $Er_2Mo_3Si_4$ buttons were reduced to a powder 100 μm or less in diameter. Here, the light phase is $Er_2Mo_3Si_4$ and the gray phase is $MoSi_2$.

fraction measurements of the grain boundary layer indicated a eutectic composition of $Er_2Mo_3Si_4$–39 vol.% $MoSi_2$. Fracture of the arc-melted material indicated a strong interface between $MoSi_2$ and $Er_2Mo_3Si_4$ since most cracks were continuous with little or no crack deflection at the $MoSi_2/Er_2Mo_3Si_4$ interface. It should be noted that very few Er_2O_3 particles were seen in the arc-melted buttons and when present were only at the bottom (chill side) of the button.

It is most likely that the formation of Er_2O_3 occurred during the arc-melting stage of processing either as a result of Er reacting with residual oxygen in the argon atmosphere or by a reduction of SiO_2. A molten glassy phase was periodically seen forming as a slag on the liquid metal pool which subsequently rolled to the bottom of the button. As the button solidified, small fractions of this slag may have been trapped on the bottom side of the button. Prior to ball-milling the surfaces of all the buttons were ground to remove any surface slag. If, however, the oxide was trapped inside the button, grinding would not have removed it. Some of the $MoSi_2$ and $Er_2Mo_3Si_4$ buttons were broken up prior to mixing and remelting, and examined using scanning electron microscopy (SEM)/XEDS. Several particles were found to be Er-rich with only trace amounts of Si and Mo (Fig. 2(a)). After ball-milling for 48 h the powder size was reduced to less than 100 μm.

It is difficult to predict a possible reaction path for the reduction of SiO_2 during processing since there is no thermodynamic data available for the formation of $Er_2Mo_3Si_4$. However, since the free energy of formation of Er_2O_3 is much greater than that of the other phases present for $T \geqslant 298$K (*e.g.*, $\Delta G°_f = -1808$ kJ mol^{-1} *vs.* -856 kJ mol^{-1} for Er_2O_3 and SiO_2 respectively [20]), it may be assumed that Er_2O_3 will form and remain stable with respect to the other phases at most temperatures of interest.

The microstructures of the hot-pressed composites are shown in Fig. 3 and the volume fractions and

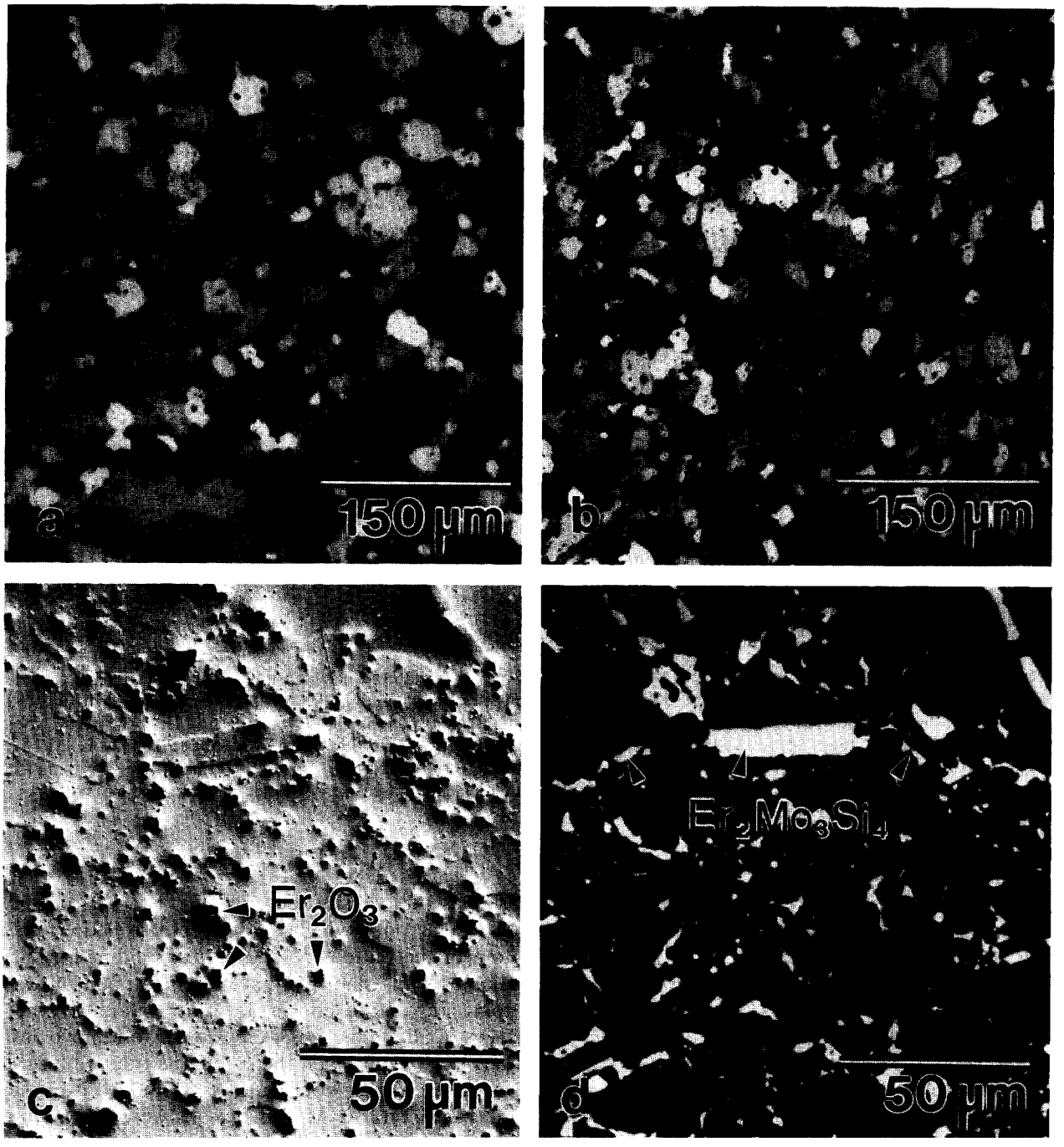

Fig. 3. Microstructures of the (a) $MoSi_2/(Er_2Mo_3Si_4/Er_2O_3)/15p$ composite hot pressed at 1650 °C and (b) the $MoSi_2/(Er_2Mo_3Si_4/Er_2O_3)/18p$ composite hot pressed at 1565 °C. Both images were recorded under cross-polarized lighting. The average grain sizes were 16 μm in (a) and 9 μm in (b). A Nomarski interference contrast image (c) and a backscattered electron image (d) of the composite hot pressed at 1565 °C showing the constituent phases of the composites. In (d) the $MoSi_2$ matrix is dark, while the Mo_5Si_3 particles are gray in color. The lighter phases in (d) are both $Er_2Mo_3Si_4$ and Er_2O_3.

particle sizes of the constituent phases are listed in Table 1. Some of the various physical properties of these constituent phases are listed in Table 2. The Er_2O_3 is seen clearly in the Nomarski interference-contrast image (Fig. 3(c)), while the $Er_2Mo_3Si_4$ can best be seen in the BSE image (Fig. 3d). The larger dispersed particles are mostly located on the $MoSi_2$ grain boundaries; however, smaller particles are also present within the $MoSi_2$ grains. Although the presence of SiO_2 was not easily detected during the metallographic study, a few silica particles were seen in both SEM and TEM (Fig. 4). In nearly every SiO_2 particle examined using TEM the SiO_2 contained second phase particles and was crystalline rather than glassy. The composition of the second phase particles was not determined, but these are believed to be Er_2O_3 or XEr_2O_3-$YSiO_2$ particles within a SiO_2 matrix. This belief is based on the known Er_2O_3-SiO_2 phase diagram that shows three line compounds ($Er_2O_3 \cdot SiO_2$, $2Er_2O_3 \cdot SiO_2$, and $Er_2O_3 \cdot SiO_2$) existing

TABLE 1. Volume fraction and particle sizes of various phases present (95% confidence)

Phase	Volume fraction (%)	Particle size (μm)
Hot pressed at 1565 °C/30 MPa/4 h		
$MoSi_2$	Bal.	9.8 ± 0.7
$Er_2Mo_3Si_4$	11.9 ± 1.8	4.2 ± 1.0
Er_2O_3	3.7 ± 1.1	2.2 ± 0.2
SiO_2	1.5 ± 0.6	—
Mo_5Si_3	1.3 ± 0.6	—
Total reinforcement	$\approx 18\%$	
Hot pressed at 1650 °C/30 MPa/4 h		
$MoSi_2$	Bal.	16 ± 1.3
$Er_2Mo_3Si_4$	7.6 ± 1.4	5.4 ± 2.6
Er_2O_3	5.1 ± 0.34	2.6 ± 1.1
SiO_2	0.25 ± 1.35	2.4 ± 2.1
Mo_5Si_3	1.1 ± 0.07	3.7 ± 1.9
Total reinforcement	$\approx 15\%$	

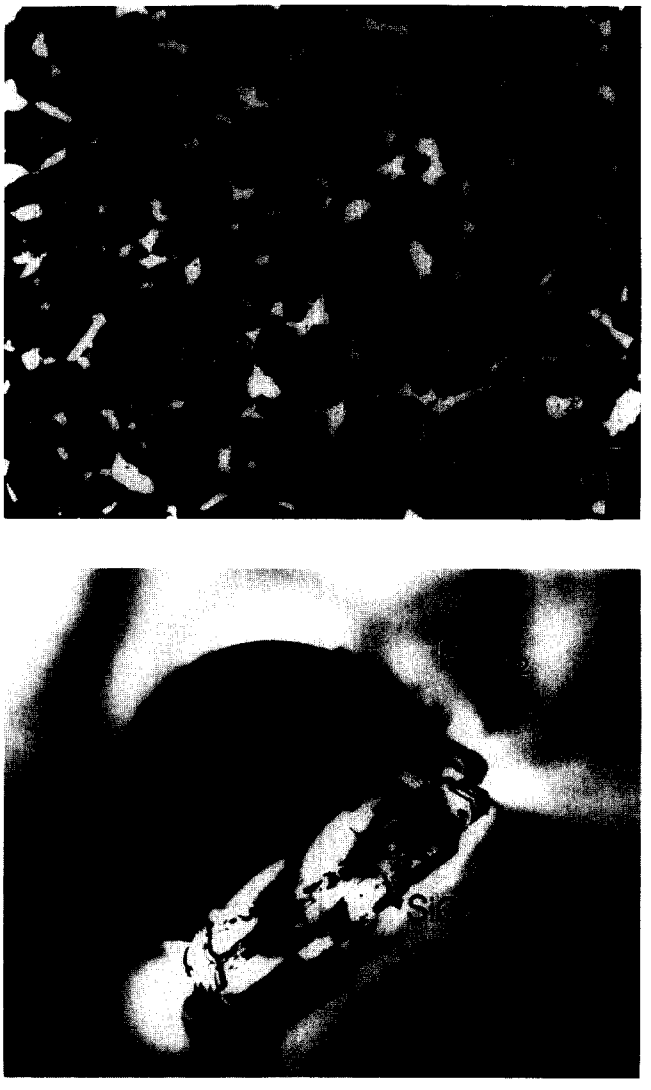

Fig. 4. (a) Backscattered electron image of the $MoSi_2$/($Er_2Mo_3Si_4$/Er_2O_3)/15p composite showing an SiO_2 particle within the matrix, and (b) TEM bright field image of an SiO_2 particle adjacent to an Er_2O_3 particle. The small second phase particles seen in the SiO_2 are believed to be intermediate phases identified in the Er_2O_3-SiO_2 phase diagram. The SiO_2 is faceted and displays diffraction contrast indicating that it is crystalline in nature.

TABLE 2. Some physical properties of the constituent phases

	$MoSi_2$	$Er_2Mo_3Si_4$	Er_2O_3	Mo_5Si_3	SiO_2
Crystal structure	Tetragonal	Monoclinic	Cubic	Tetragonal	Polymorphic
Lattice parameter (Å)	$a = 3.20$ $c = 7.85$	$a = 6.67$ $b = 6.89$ $c = 6.81$	10.55	$a = 9.65$ $c = 4.91$	—
Theoretical density (g/cc)	6.25	8.25	8.62	8.2	2.65
Melting temperature (°C)	2020	≈ 1930	2345	2180	1695 (glass softens ≈ 1250)
CTE ($\times 10^{-6}$ °C^{-1})	8.5	Unknown	8.6	6.7	0.55 (quartz glass)

below 1680 °C with eutectic invariants existing between neighboring phases in the diagram [21]. The presence of these second phase particles, and the crystalline nature of the SiO_2 should increase the viscosity of the silica-rich phase if present on the $MoSi_2$ grain boundaries.

A typical Er_2O_3 particle is shown in the bright field TEM image in Fig. 5. The STEM/XEDS spectrum in Fig. 5(b) shows the composition of this phase to be Er-rich with an oxygen Kα peak occurring at 523 eV. Convergent beam electron diffraction (CBED) patterns from the [001], [011] and [111] zones axes of an Er_2O_3 particle are shown in Figs. 6–8. The tilt angles recorded from the microscope goniometers, and the interplanar spacings and angles determined from

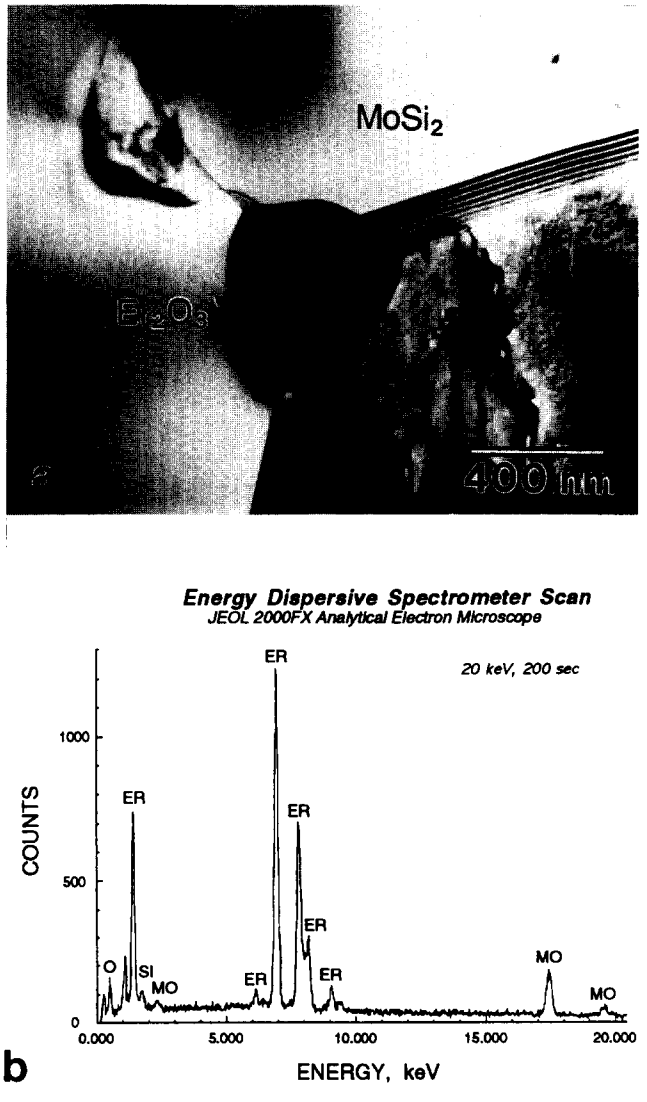

Fig. 5. (a) TEM bright field image showing a typical Er_2O_3 particle located at a grain corner. (b) Many particles were identified by STEM/XEDS as Er-rich, containing oxygen (peak at 523 eV).

corresponding selected area diffraction patterns (SADPs) were consistent with those reported in the literature for cubic Er_2O_3 [22, 23]. Upon further examination of the CBED patterns according to Buxton *et al.* [24], the whole pattern (WP) and bright field disk (BF) symmetries of the crystalline oxide are seen to be *2mm* for the [001] zone, *m* for the [011] zone, and *3* for the [111] zone. The possible diffraction groups listed for these symmetries are *2mm* and $2mm1_R$ for the [001] zone, *m* and 2_Rmm_R for the [011] zone, and *3* and 6_R for the [111] zone. An analysis of the zero order Laue zones (ZOLZ) of the [111] and [011] patterns reveal that the diffraction groups are 6_R and 2_Rmm_R respectively. It is important to note that higher order (HOLZ) information within the disks of the zero order layer must be ignored when determining the symmetry of a ZOLZ pattern. An area of appropriate thickness should be selected such that the HOLZ information within the disks is minimized or else the symmetry of the pattern may be incorrectly identified. The only crystal point group consistent with all three zones is $m\bar{3}$ as reported for Er_2O_3 [21, 25].

The space group was determined by examining the Gjonnes–Moodie (GM) lines in the dynamically forbidden reflections of the [011] ZOLZ pattern [26,27]. An A_2 GM line is present in the $0\bar{1}1$ reflection of the [011] zone axis pattern and is seen to repeat at each odd reflection along the mirror line indicating the presence of an *a*-glide plane. When tilted to exactly excite the $03\bar{3}$ reflection (Fig. 9), B_2 and A_3 GM lines also appear in the *033* reflection. The unit cell was determined by projecting the first order Laue zone reflections onto the zero order layer. The resulting three dimensional lattice indicated either a face-centered cubic (f.c.c.) or body-centered cubic (b.c.c.) reciprocal lattice. The height of the reciprocal lattice in the beam direction was determined by measuring the diameter of the first order ring. The ratio of the height of the reciprocal lattice to the shortest reciprocal lattice vector in the zero order pattern was then calculated and this indicated an f.c.c. reciprocal lattice or b.c.c. real lattice. This information, accompanied with an analysis of all three zone axis patterns, is consistent only with the space group $Ia\bar{3}$ which is the reported space group for Er_2O_3 [21, 24].

Hot hardness values for the monolithic materials and the particulate composite are shown in Fig. 10. The fact that the hardness of $Er_2Mo_3Si_4$ dropped only slightly from about 9.2 GPa at room temperature to roughly 6 GPa at 1300 °C served as the basis for choosing $Er_2Mo_3Si_4$ as the primary reinforcement phase for $MoSi_2$. The high strength of $Er_2Mo_3Si_4$ at high temperature may be attributed to its monoclinic crystal structure [21, 22] and the lack of available slip systems for this crystal structure. In addition, the

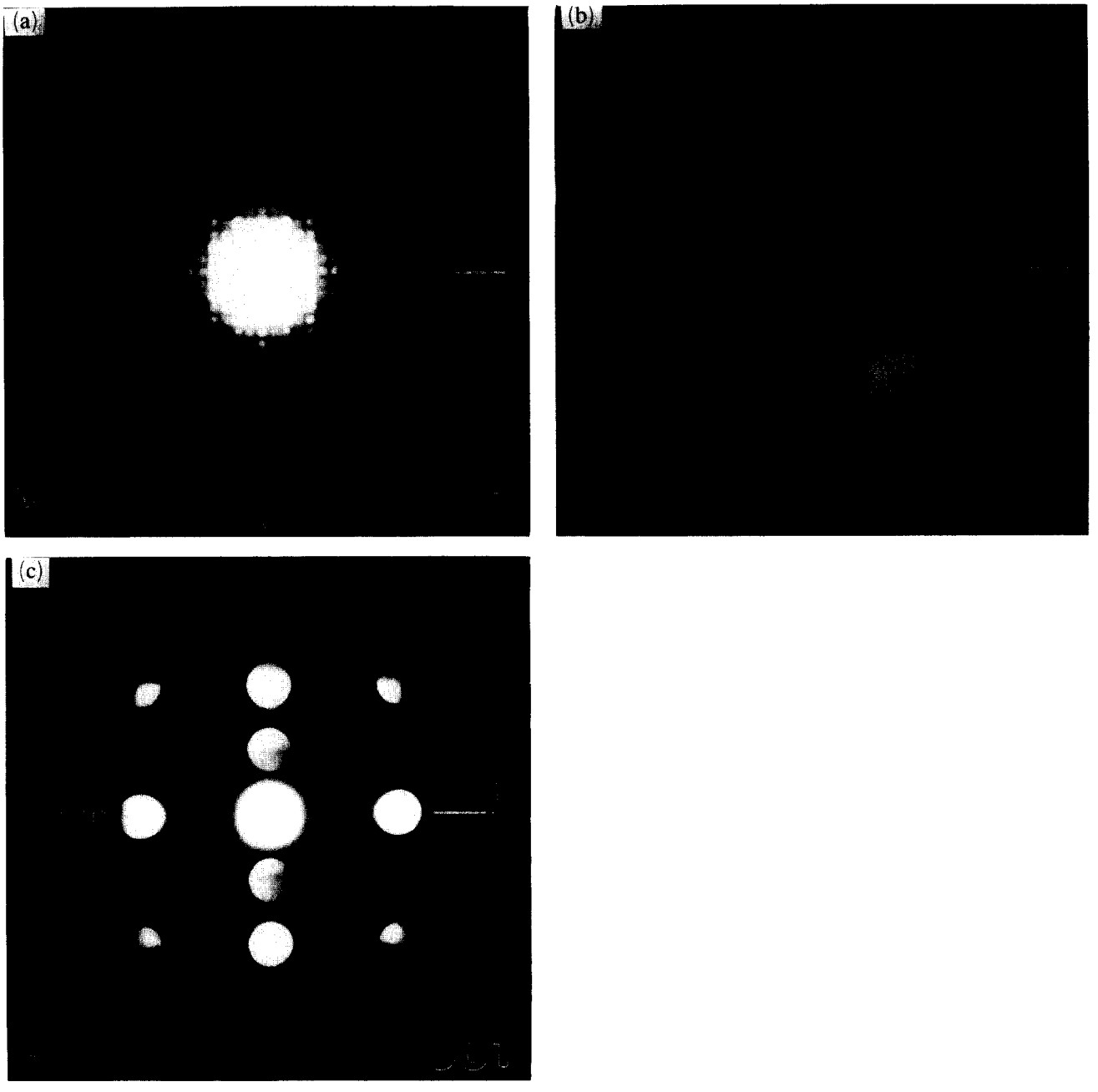

Fig. 6. Convergent beam electron diffraction (CBED) patterns of the [001] zone axis of Er_2O_3. The whole pattern (WP), bright-field disk (BF), and zero order Laue zone (ZOLZ) symmetries are *2mm*. The possible diffraction groups accordng to Buxton *et al.* [23] are *2mm* and $2mm1_R$.

formation of Er_2O_3 during the various stages of processing enhanced the possibility of improving the mechanical properties by reducing the volume fraction of the low viscosity grain boundary siliceous phase and introducing a thermodynamically stable, crystalline oxide phase as an additional reinforcement.

The results of compressive decremental step-strain tests are shown in Fig. 11. The flow stress dependence on the applied strain rate for these $MoSi_2$ composite materials was found to follow a power-law relationship. The stress exponent, n, of the constitutive equation for power-law creep behavior was found to be temperature dependent with n equal to 5 at 1100 °C and 1200 °C, and 3.9 at 1300 °C for the larger grain size material. At 1400 °C stress exponents of 2.0 at strain rates below 10^{-4} and 4.4 at strain rates above 10^{-4} were determined for this material. Values of n greater than 3 have been associated with dislocation glide-climb controlled creep processes. Based on this response and the proposed models for dislocation

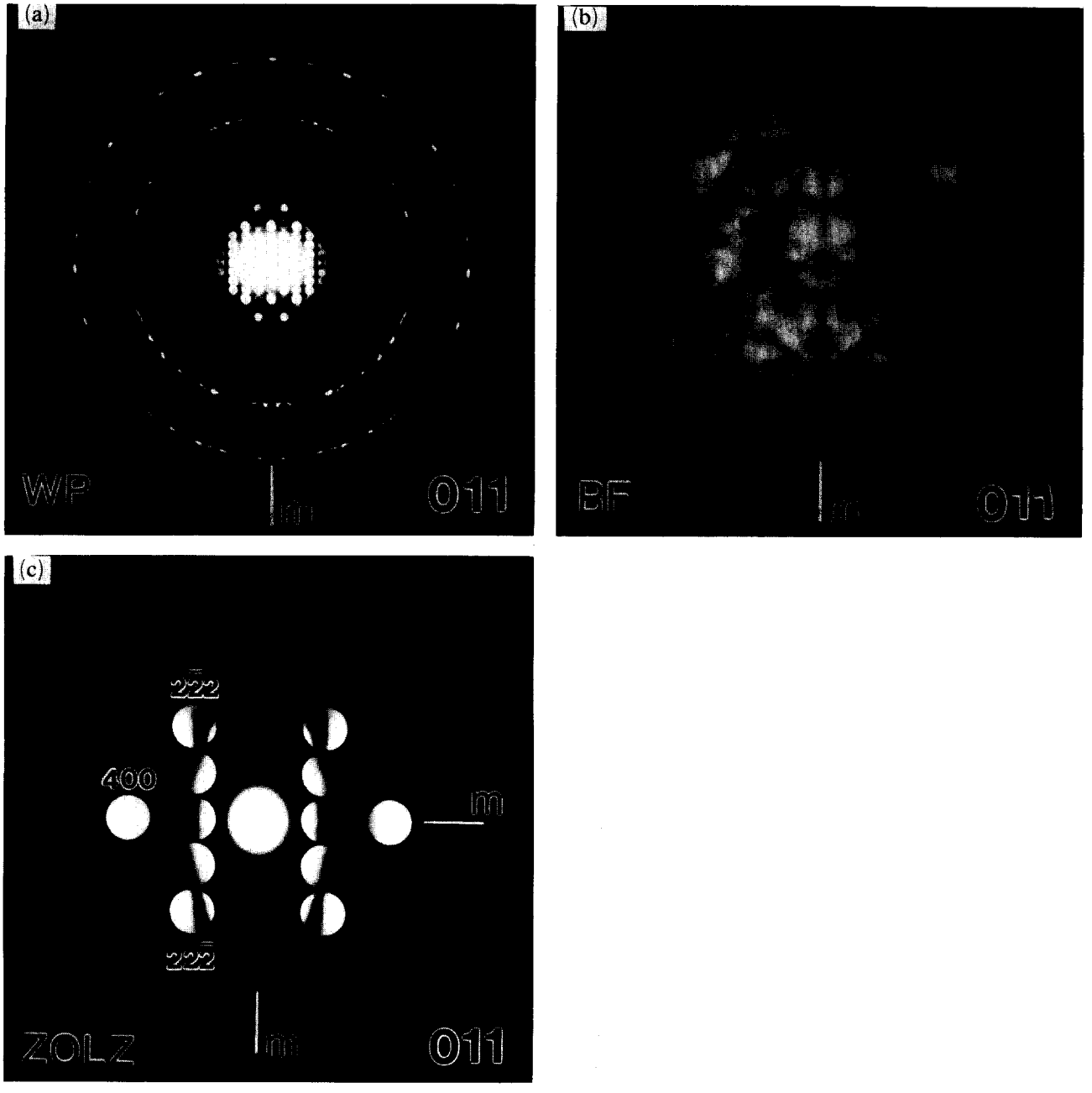

Fig. 7. Convergent beam electron diffraction (CBED) patterns of the [011] zone axis of Er_2O_3. The whole pattern (WP) and bright-field disk (BF) symmetries are *m*, while the symmetry of the ZOLZ pattern is *2mm*. The only possible diffraction group is $2_R mm_R$.

creep we believe that the drop in the stress exponent, with increasing temperature or decreasing strain rate, indicates an increased contribution from grain boundary sliding at higher temperatures. Above about 1200 °C, two mechanisms (dislocation creep and grain boundary sliding) are believed to be operating. At 1300 °C, a lower stress exponent was observed for the smaller grain size material indicating that a transition in creep behavior may occur at a lower temperature for a smaller grain size, *i.e.* between 1200 °C and 1300 °C. This observation would be consistent with the results of Suzuki *et al.* [9] who reported a change in the creep activation energy at about 1170 °C for a fine grained SiC-reinforced XD™ $MoSi_2$. The stress exponent of

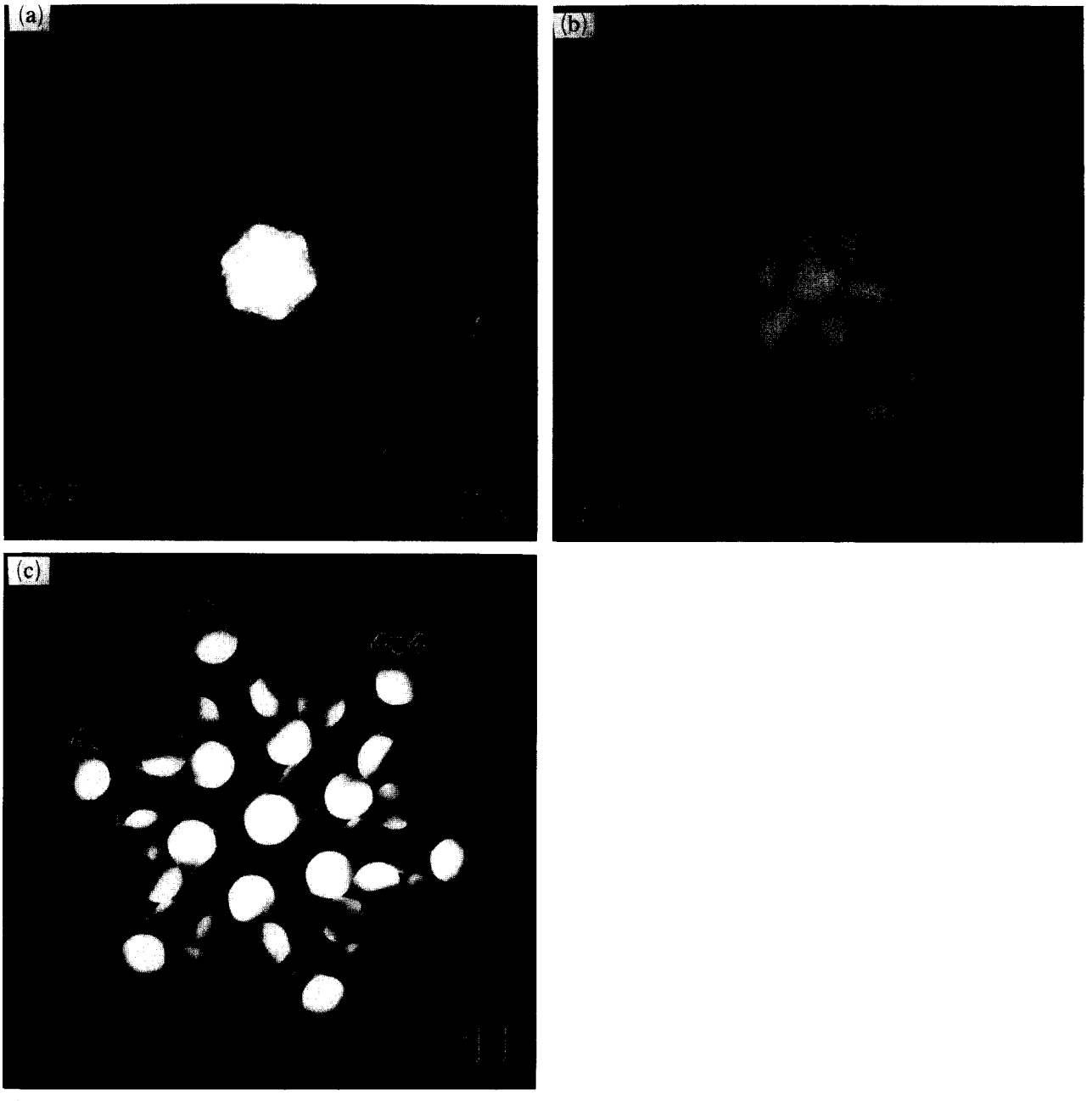

Fig. 8. Convergent beam electron diffraction (CBED) patterns of the [111] zone axis of Er_2O_3. The whole pattern (WP) and bright-field disk (BF) symmetries are *3*, while the symmetry of the ZOLZ pattern is *6*. The diffraction group is 6_R.

1.7 at 1300 °C for the 9 μm material is similar to that reported by Sadananda *et al.* [17] for monolithic powder-processed $MoSi_2$ in this temperature range.

A grain size dependent creep strength became apparent between the two billets tested in this study (Fig. 11(b)). All attempts to determine the cause of the discrepancy between the data recorded here at 1300 °C and that previously reported by the authors [16] proved to be inconclusive. Further testing of samples from the same billet resulted in strengths considerably lower than that previously reported. The material hot-pressed at 1565 °C, with a grain size of 9 μm, shows lower strength and a lower stress exponent at 1300 °C than that of the larger grain size material (16 μm) which was hot-pressed at 1650 °C. This indicates that the creep rate is affected more by diffusional processes in the smaller grain size material. It should be noted that a minor difference in the volume fraction of the reinforcement phases exists between the two materials tested here. The size of the

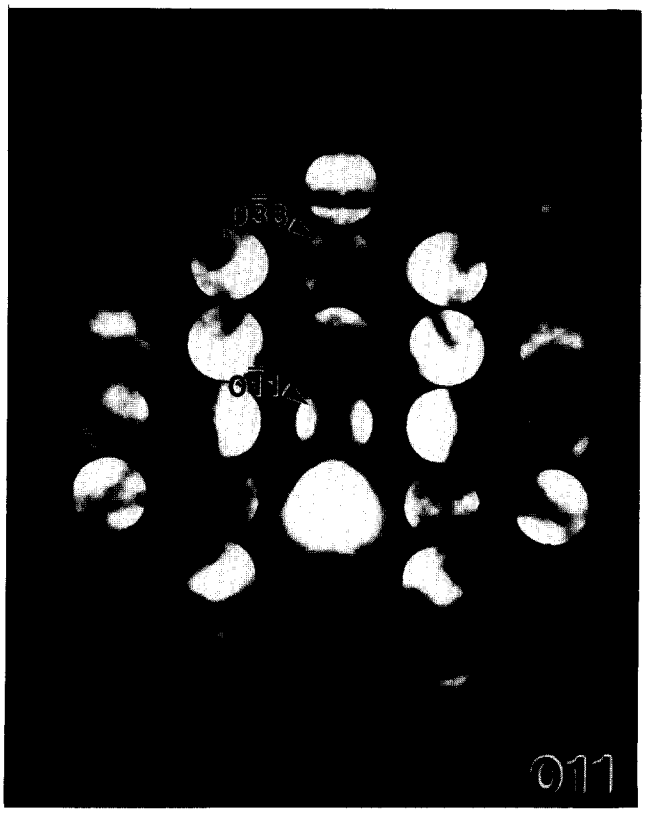

Fig. 9. Convergent beam electron diffraction pattern of the [011] zone axis tilted to excite the $0\bar{3}3$ reflection. The presence of A_2 Gjonnes-Moodie lines in the $0\bar{1}1$ reflection, and B_2 and A_3 lines in the 033 reflection of the [011] ZOLZ pattern uniquely identifies the Er_2O_3 space group as $Ia\bar{3}$ in agreement with literature [21, 24].

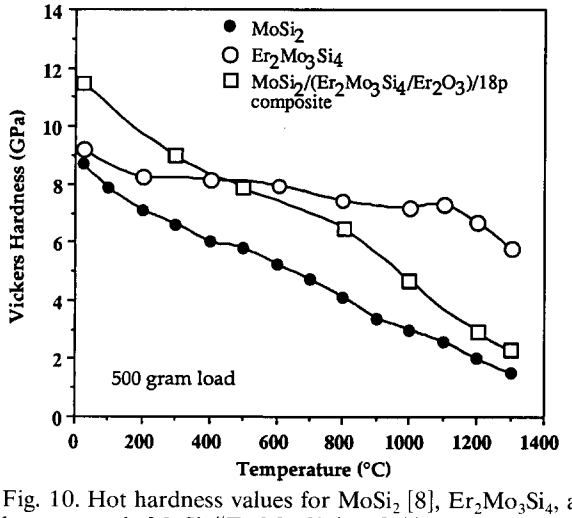

Fig. 10. Hot hardness values for $MoSi_2$ [8], $Er_2Mo_3Si_4$, and the hot pressed $MoSi_2/(Er_2Mo_3Si_4/Er_2O_3)/18p$ composite. The hardness of this composite is similar to that reported by Maloy *et al.* [8] for $MoSi_2$ + 2wt.%C.

reinforcement particles is slightly smaller and the volume fraction of the reinforcing phases is higher in the smaller grain size material. Again, this difference in the reinforcement would indicate that the grain size

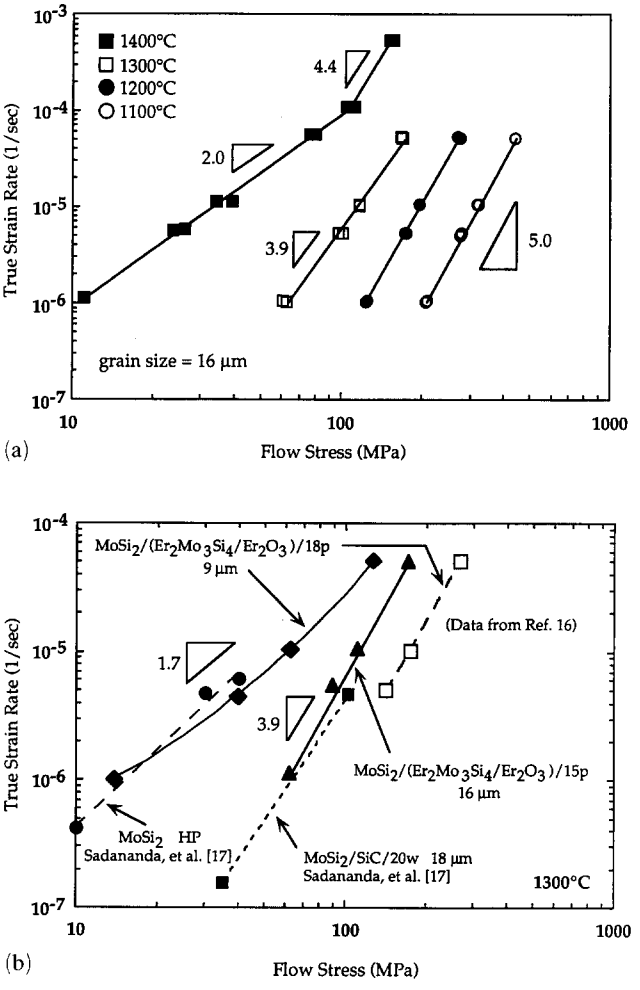

Fig. 11. (a) Results of decremental step-strain rate tests for the 16 μm grain size $MoSi_2/(Er_2Mo_3Si_4/Er_2O_3)/15p$ composite. The stress exponent decreases with increasing temperature as expected due to increasing contributions from diffusional processes. It appears that dislocation climb becomes the dominant mechanism as temperature increases from 1100 °C to 1300 °C. Above 1300 °C grain boundary diffusional flow accompanied by grain boundary sliding begins to dominate over dislocation climb-glide as the rate controlling mechanism. (b) Data from step-strain rate tests conducted on both the 16 mm and the 9 μm grain size materials at 1300 °C shows the grain size dependence of creep strength. A decrease in the stress exponent at smaller grain sizes is indicative of a transition in the controlling mechanism for creep.

was more influential than the interparticle spacing in determining the creep resistance. A grain size dependent creep strength has also been reported recently by Basu and Ghosh [28] for $MoSi_2/CaO/15p$ composites.

The activation energy for creep, Q, was determined by a regression analysis using the method of least squares applied to two separate types of data plots. In Fig. 12 the Zener-Hollomon parameter ($\dot{\varepsilon} \exp(Q/RT)$) is plotted as a function of the flow stress at the var-

ious test temperatures. An activation energy of approximately 435 kJ mol^{-1} was determined by this method. Fig. 13 is an Arrhenius plot of true strain rate *vs.* reciprocal temperature for a constant flow stress of 200 MPa. The slope of curve is equal to $(-Q/R)$ and the activation energy was determined to be 415 kJ mol^{-1}. This range of activation energy is consistent with that found in the literature and is indicative of climb of edge dislocations controlled by diffusion of Mo in $MoSi_2$ [17, 18, 29].

The increase in creep resistance for the composite over that of monolithic $MoSi_2$ may be attributed not only to the presence of small dispersed particles in the interior of the $MoSi_2$ grains (inhibiting dislocation motion), but more importantly to the presence of these hard particles along the $MoSi_2$ grain boundaries and grain corners which would reduce grain sliding. The above results indicate that the creep resistance at low temperatures or high strain rates is dislocation climb and glide controlled; however, at higher homologous temperatures grain boundary sliding makes a significant contribution to the creep rate.

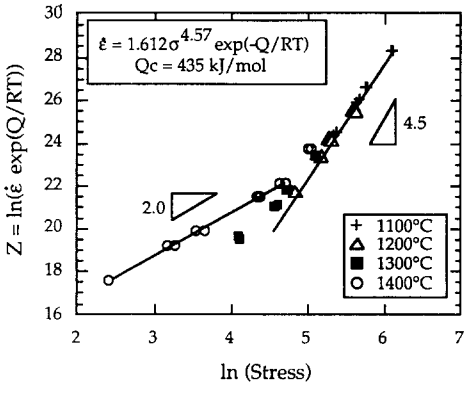

Fig. 12. A plot of the Zener–Holloman parameter (Z) for the 16 μm grain size material. A best-fit curve resulted in a creep activation energy of 435 kJ mol^{-1}. A transition in the creep controlling mechanism occurs at temperatures above 1200 °C.

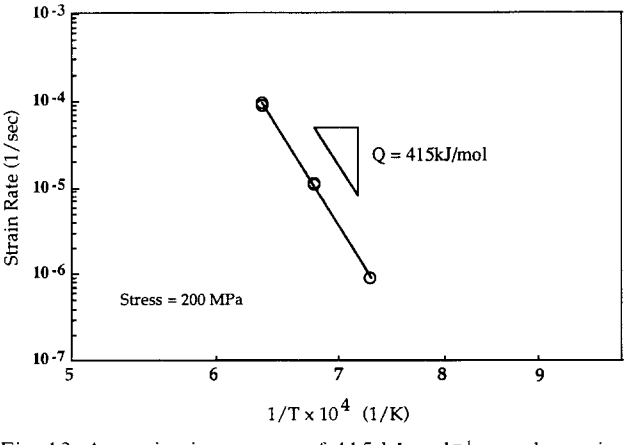

Fig. 13. An activation energy of 415 kJ mol^{-1} was determined for the 16 mm grain size composite by an Arrhenius plot of the data in the temperature range for dislocation controlled creep.

A closer examination of Fig. 12 reveals a greater deviation of the data from the curve fit in the low-stress (higher temperature) region for the 16 μm material. In our previous investigation [16] the stress exponent at 1200 °C was reported to be 3.3 for the composite prepared at 1565 °C (9 μm) while the exponent was approximately 5 for the 16 μm material examined in this study. The strengths, however, are similar. The reduced stress exponent in the smaller grain size material may indicate that creep deformation is dominated more by dislocation glide up to 1200 °C, since the strength is similar to that of the 16 μm material, but grain boundary diffusion and/or grain sliding is beginning to play a more substantial role in the deformation at temperatures above 1200 °C. This transition in the rate controlling mechanisms would be expected to occur at higher temperatures for the larger grained material and, indeed, this was observed.

We believe the formation of Er_2O_3 at the expense of SiO_2 significantly decreased the amount of any viscous grain boundary phase in these composites. Under an applied stress at elevated temperatures, any SiO_2 present along the boundaries or at grain corners would enhance grain boundary sliding since the SiO_2 would deform by a viscous shear process. The reduction of SiO_2 and subsequent formation of thermodynamically stable, non-deformable particles would significantly reduce this contribution. However, at yet higher temperatures diffusion around these hard barriers [30] would again produce grain sliding which may be present at 1400 °C for the 16 μm material at the slower strain rates.

Sadananda and Feng [31] have examined the effect of back stresses in monolithic $MoSi_2$ and $MoSi_2$/SiC/20p composites. They considered the resulting effective stress (applied stress–back stress) in their calculations and found that although the contribution from the back stresses was more pronounced in the composite materials than in the monolithic material, and increased more rapidly in the composites with decreasing temperature, this contribution was minimal and did not significantly change the stress exponent or the creep activation energy. This finding is somewhat expected since in most oxide dispersion alloys the back stress is attributed more to dislocation interactions with the dispersoids. Furthermore, in the present study it was clear that grain size was more influential since the material with the smaller grain size had a higher number density of second phase particles.

It should also be noted that intergranular cracking was more prominent at the lower test temperatures.

Optical micrographs of samples deformed at 1100 °C and 1300 °C are shown in Fig. 14. The large dark areas in the 1100 °C sample (Fig. 14(a)) are voids created by particles or grains being removed or "falling out" during the metallographic polishing process. This indicates that a substantial amount of intergranular cracking was present in the 1100 °C sample. Above 1300 °C, the crack density is much less, indicating that grain boundary sliding is accompanied by diffusional mass flow, allowing the boundaries to remain intact (Fig. 14(b)).

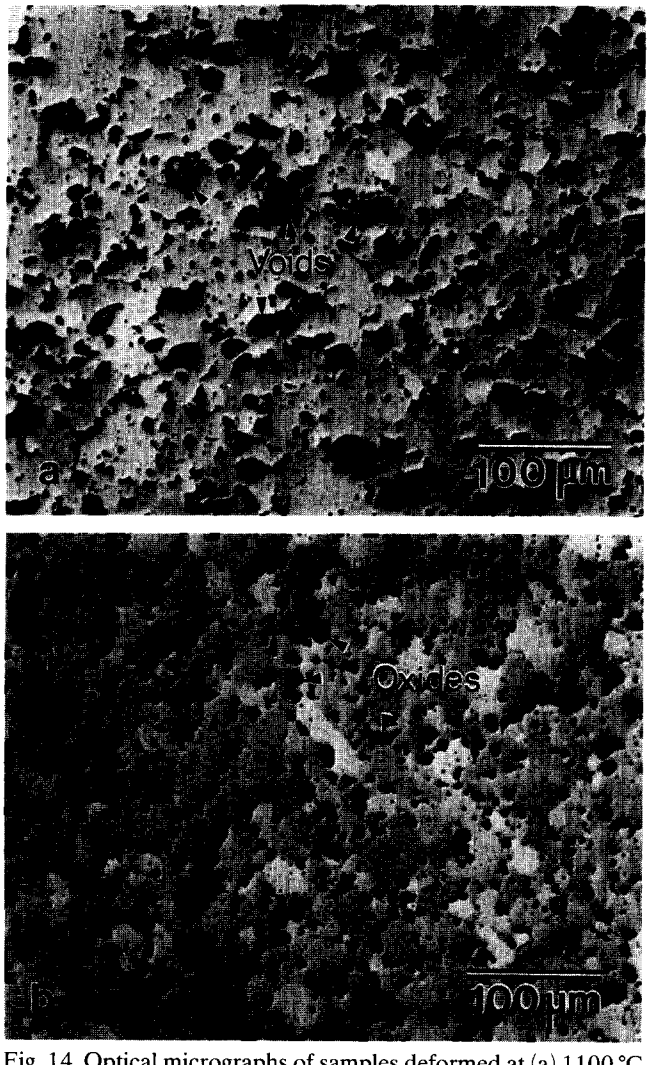

Fig. 14. Optical micrographs of samples deformed at (a) 1100 °C and (b) 1300 °C. The large voids in the 1100 °C sample are a result of particles or grains being removed from the sample during polishing. Both samples were prepared simultaneously by the same metallographic technique. This indicates that more intergranular cracking was present in the sample deformed at the lower temperature. At 1300 °C, grain boundary sliding accompanied by diffusional mass flow allows the boundaries to remain intact. The small particles seen in (b) are oxides.

4. Summary

A simple processing scheme was found to produce $MoSi_2$ composites that had reduced levels of SiO_2. The presence of $Er_2Mo_3Si_4$ was found to increase the creep strength of $MoSi_2$ due to its retention of hardness and strength at elevated temperatures. The addition of erbium to the starting material also led to the formation of Er_2O_3, a thermodynamically stable, crystalline oxide. The reduction in SiO_2 content, as well as the presence of Er_2O_3 particles is also believed to have contributed to an increase in creep resistance. A transition in the creep controlling mechanism was observed above 1200 °C which was indicated by a decrease in the stress exponent with increasing temperature or decreasing strain rate. It was also shown that the creep strength of $MoSi_2$ is grain size dependent with creep resistance increasing with larger grain size.

Acknowledgments

The authors wish to express their thanks to Dr. J. F. Mansfield and Mr. Carl Henderson of the University of Michigan Electron Microbeam Analysis Laboratory for their assistance, and Profs. A. K. Ghosh and R. Gibala for permitting the use of the equipment used to obtain the mechanical property data. This research was funded by the National Science Foundation, Grant No. MSM 86-57581.

References

1 F.D. Gac and J.J. Petrovic, *J. Am. Ceram. Soc. 68* (8) (1985) C200–C201.
2 J.D. Cotton, Y.S. Kim and M.J. Kaufman, *Mater. Sci. Eng., A 144* (1991) 287–291.
3 R.B. Schwartz, S.R. Srinivasan, J.J. Petrovic and C.J. Maggiore, *Mater. Sci. Eng., A 155* (1992) 75–83.
4 A.W. Searcy, *J. Am. Ceram. Soc., 40* (12) (1957) 431–435.
5 J.B. Berkowitz-Mattuck and R.R. Dils, *J. Electrochem. Soc. 112* (6) (1965) 583–589.
6 C.D. Wirkus and D.R. Wilder, *J. Am. Ceram. Soc., 49* (4) (1966) 173–177.
7 R. Gibala, A.K. Ghosh, D.C. Van Aken, D.J. Srolovitz, A. Basu, H. Chang, D.P. Mason and W. Yang, *Mater. Sci. Eng., A 155* (1992) 147–158.
8 S.A. Maloy, J.J. Lewandowski, A.H. Heuer and J.J. Petrovic, *Mater. Sci. Eng., A 155* (1992) 159–163.
9 M. Suzuki, S.R. Nutt and R.M. Aikin, Jr., in D.B. Miracle, D.L. Anton and J.A. Graves (eds.), *Intermetallic Matrix Composites II*, Materials Research Society Symposia Proceedings, Materials Research Society, Pittsburgh, PA, 1992, Vol. 273, pp. 267–274.
10 S. Jayashankar and M.J. Kaufman, *Scripta Metall., 26* (1992) 1245–1250.
11 D.A. Hardwick, P.L. Martin and R.J. Moores, *Scripta Metall., 27* (1992) 391–394.

12 D.P. Mason, D.C. Van Aken and J.F. Mansfield, in D.B. Miracle, D.L. Anton and J.A. Graves (eds.), *Intermetallic Matrix Composites II*, Materials Research Society Symposia Proceedings, Materials Research Society, Pittsburgh, PA, 1992, Vol. 273, pp.289–294.
13 D.P. Mason, Ph.D. Thesis, The University of Michigan, 1994.
14 J.J. Petrovic, A.K. Bhattacharya, R.E. Honnell, T.E. Mitchell, R.K. Wade and K.J. McClellan, *Mater. Sci. Eng., A155* (1992) 259–266.
15 Y.S. Kim, M.R. Johnson, R. Abbaschian and M.J. Kaufman, in L.A. Johnson, D.P. Pope and J.O. Stiegler (eds.), *High Temperature Ordered Intermetallic Alloys IV*, Materials Research Society Symposia Proceedings, Materials Research Society, Pittsburgh, PA, 1991, Vol. 213, pp. 839–845.
16 D.K. Patrick and D.C. Van Aken, in I. Baker, J.D. Whittenberger, R. Darolia and M.H. Yoo (eds.), *High Temperature Ordered Intermetallic Alloys V*, Materials Research Society Symposia Proceedings, Materials Research Society, Pittsburgh, PA, 1993, Vol. 288, pp. 1135–1141.
17 K. Sadananda, C.R. Feng, H. Jones and J. Petrovic, *Mater. Sci. Eng., A155* (1992) 227–239.
18 S. Bose, *Mater. Sci. Eng., A155* (1992) 217–225.
19 J.E. Hilliard and J.W. Cahn, *Trans. TMS-AIME, 221* (1961) 344.
20 I. Barin, *Thermochemical Data of Pure Substances*, VCH Publishers, Germany, 1989.
21 E.M. Levin, C.R. Robbins and H.F. McMurdie, *Phase Diagrams for Ceramists*, 1969 Supplement, American Ceramic Society, Inc., Columbus, OH, p. 100, Fig. 2365.
22 P. Villars and L.D. Calvert, *Pearson Handbook of Crystallography Data for Intermetallic Phases*, ASM International, Metals Park, OH, 1991, 2nd edn., Vol. 3, p. 3130 and p. 3138.
23 J.L.C. Daams, P. Villars, and J.H.N. van Hucht, *Atlas of Crystal Structure Types for Intermetallic Phases*, ASM International, Metals Park, OH, 1991, p. 319 and p. 6706.
24 B.F. Buxton, J.A. Eades, J.W. Steeds and G.M. Rackham, *Philos. Trans. Roy. Soc. Lond., 281* (1301) (1976) 171–194.
25 T. Hahn (ed.), *International Tables for Crystallography*, Reidel, Holland, 1983, Vol. A.
26 J. Gjonnes and A.F. Moodie, *Acta Cryst., 19* (1965) 65–67.
27 M. Tanaka, H. Sekii and T. Nagasawa, *Acta Cryst., A39*, (1983) 825–837.
28 A. Basu and A.K. Ghosh, in N.S. Stoloff, D.J. Duquette and A.F. Giamei (eds.), *Critical Issues in Development of High Temperature Structural Materials*, TMS, Pittsburgh, PA, 1993.
29 S.M. Wiederhorn, R.J. Gettings, D.E. Roberts, C. Ostertag and J.J. Petrovic, *Mater. Sci. Eng., A155* (1992) 209–215.
30 T.H. Courtney, *Mechanical Behavior of Materials*, McGraw-Hill, New York, 1990, p. 280.
31 K. Sadananda and C.R. Feng, *presented at the Symposium on Processing, Fabrication, and Performance of Composite Materials II*, ASME Winter meeting, Anaheim, CA, 1992.